High Brightness HDR Projection Using Dynamic Freeform Lensing

GERWIN DAMBERG and JAMES GREGSON
University of British Columbia
and
WOLFGANG HEIDRICH
King Abdullah University of Science and Technology
and University of British Columbia

Cinema projectors need to compete with home theater displays in terms of image quality. High frame rate and spatial resolution as well as stereoscopic 3D are common features today, but even the most advanced cinema projectors lack in-scene contrast and more importantly high peak luminance, both of which are essential perceptual attributes of images appearing realistic. At the same time, HDR image statistics suggest that the average image intensity in a controlled ambient viewing environment such as cinema can be as low as 1% for cinematic HDR content and not often higher than 18%, *middle gray* in photography. Traditional projection systems form images and colors by blocking the source light from a lamp, therefore attenuating on average between 99% and 82% of light. This inefficient use of light poses significant challenges for achieving higher peak brightness levels.

In this work, we propose a new projector architecture built around commercially available components, in which light can be steered to form images. The gain in system efficiency significantly reduces the total cost of ownership of a projector (fewer components and lower operating cost) and at the same time increases peak luminance and improves black level beyond what is practically achievable with incumbent projector technologies. At the heart of this computational display technology is a new projector hardware design using phase-modulation in combination with a new optimization algorithm that is capable of on-the-fly computation of freeform lens surfaces.

Categories and Subject Descriptors: I.3.3 [**Computer Graphics**]: Three-Dimensional Graphics and Realism—*Display Algorithms*

General Terms: Freeform lensing, high dynamic range projection, caustics

Additional Key Words and Phrases: Laser projector, high brightness, visual perception, image statistics, high peak luminance

ACM Reference Format:

Damberg, G., Gregson, J. and Heidrich, W. 2015. Dynamic Freeform Lensing with Application for High Brightness HDR Projection. ACM Trans. Graph. XX, X, Article XXX (MONTH 201X), 10 pages.
DOI = 10.1145/1559755.1559763
http://doi.acm.org/10.1145/ 1559755.1559763

Authors' addresses: gdamberg@cs.ubc.ca, jgregson@cs.ubc.ca, heidrich@cs.ubc.ca.

DOI 10.1145/XXXXXXX.YYYYYYY
http://doi.acm.org/10.1145/XXXXXXX.YYYYYYY

1. INTRODUCTION

Ideally, HDR projectors *should* produce both darker black and (much) brighter highlights while at the same time maintaining an appropriate-for-the-viewing-environment average picture level (APL). However, todays HDR projectors predominantly focus on improving black level (for example recently demonstrated laser projection systems by Kodak, IMAX, Zeiss, Dolby, Barco, Christie and others). Improved contrast *and* peak luminance are vital for higher perceived image quality (brightness, colorfulness) [Rempel et al. 2009]. Brightness perception of luminance levels is near-logarithmic in the photopic range. Doubling the luminance of an image feature on a projection screen (e.g. by increasing the lamp power of a traditional projector by $2\times$) does not result in a significant improvement in perceived brightness.

Results in [Rempel et al. 2011; Reinhard et al. 2012; Zink and Smith 2015] suggest that $10\times$, $20\times$ or even $100\times$ increases in peak luminance would be desirable, even if most images only require a very small percentage of pixels to be this bright (also see Section 3.1).

Such drastic improvements cannot be achieved with conventional projector designs, which use amplitude spatial light modulators (or *SLMs*) to generate images by pixel-selectively blocking light. For a typical scene, this process destroys between 82% and 99% of the light that *could* reach the screen, with the energy being dissipated as heat. This causes a number of engineering challenges, including excessive power consumption, thermal engineering, and cost, which ultimately limit the peak luminance in current projector designs.

In this paper, we explore the use of *dynamic* freeform lenses in the context of light efficient, high (local) peak luminance, and high contrast (high dynamic range, HDR) projection systems. Freeform lenses, i.e. aspherical, asymmetric lenses have recently received a lot of attention in optics as well as computer graphics. In the latter community, freeform lenses have mostly been considered under the auspices of *goal-based caustics*, i.e. the design of lenses that generate a specific caustic image under pre-defined illumination conditions [Finckh et al. 2010; Papas et al. 2011; Schwartzburg et al. 2014; Yue et al. 2014].

We implement dynamic freeform lensing on a *phase-only* SLM, which is combined with a conventional light blocking device such as a reflective LCD in a new type of cascaded modulation approach. The phase modulator in our approach creates a smooth, but still quite detailed *caustic* image on the amplitude modulator. Since the caustic image merely redistributes, or *reallocates*, light [Hoskinson et al. 2010], this approach produces both a higher dynamic range as well as an improved (local) peak luminance as compared to conventional projectors.

This work is based on our earlier work on generating freeform lenses or goal driven caustics using common approximations in optics to directly optimize the phase modulation pattern or lens shape of a freeform lens [2015]. The method will be briefly reviewed in Section 3.2. In the current work, we make the following new contributions:

—a new Fourier domain optimization approach for generating freeform lenses that is capable of high frame rates for dynamic light steering using phase modulators.

—a new dual-modulation projector design that combines one phase and one amplitude modulator for image generation and enables high brightness, high contrast images.

To our knowledge, this is both the first time that practical, high-resolution light redistribution has been shown using *commercially available* hardware, as well as the first time that phase-only SLMs have been used for dynamic freeform lensing.

2. RELATED WORK

Our research draws from a number of different fields of related work, including both display technologies and algorithms for freeform lens design. The following is a brief description of the state of the art in several related fields.

2.1 Dynamic Contrast, Irises and Global Light Source Dimming

The performance of projector systems and other types of displays is often advertised in terms of *dynamic contrast*, which relates to the sequential measurement of the intensity of a “full white” image and a “full black” image. Dynamic contrast ratings can be increased significantly with projector architectures that can globally modulate the intensity of the image, for example by dimming the light source (for solid state lighting such as LED or laser projectors), or through the use of a mechanical iris (for high pressure discharge lamps which cannot be dimmed). In product marketing material the quoted sequential contrast numbers for these types of projectors often exceed 1,000,000:1. Although projectors with high dynamic contrast provide an improved viewing experience by allowing “mood adaptations” according to image content, these numbers are not indicative of true HDR performance, since simultaneous in-scene contrast is typically only between 1,000:1 and 6,000:1. In our work we aim for true HDR projection with simultaneously brighter peak luminance and deeper black levels, while limiting power consumption.

2.2 Dual Modulation Projection Displays

Over the last two decades, there have been several different proposals to implement dual modulation approaches in display applications to increase in-scene contrast. The availability of large flat panel TVs and high power LEDs led to an adoption of dual modulation techniques in consumer electronics [Seetzen et al. 2004]. Similar concepts to increase contrast in projectors include screens with spatially varying reflectivity (either statically [Bimber and Iwai 2008] or dynamically [Seetzen 2009]), and arrays of hundreds or even thousands of primitive projectors [Seetzen 2009], proposed as means to increase on-screen luminance. Few of these concepts have made it past the research stage and small-scale prototypes. One exception are dual modulation projector designs using two traditional amplitude SLMs in sequence [Blackham and Neale 1998; Damberg et al. 2007; Damberg et al. 2007; Kusakabe et al. 2009]. These systems are typically intended for specialty applications requiring very good black level and limited peak luminance. The low optical efficiency of amplitude SLMs results in both a low light intensity on screen and high power consumption, all at significantly increased system cost. Nevertheless dual amplitude attenuating projectors are being deployed not only in planetariums, training and simulation applications, but recently also in high end, *premium large format*, cinema.

To alleviate the problem of inefficient image formation, Hoskinson et al. [2010; 2012] introduced the notion of *light reallocation* using 2D arrays of tip-tilt mirrors in the light path of a small DLP projector, whereby the first modulator does not actually absorb much light, but moves it around within the image plane, so it can be reallocated from dark image regions to bright ones, essentially creating moving, bright spots of approximately constant size on the amplitude modulator. Hoskinson and co-authors used a continuously tilting micro-mirror array to achieve this light reallocation. Unfortunately such mirror arrays are not easy to control accurately (achieving predictable tile-angles for a given drive signal) and are still only available as research prototypes at low spatial resolution (7×4 pixels in their work).

In our work, we achieve high contrast light steering by employing a readily available 2 megapixel LCoS SLM operated in a phase-only fashion. Instead of computationally determining independent mirror tilt angles, we optimize a continuous phase function representing the required curvature of the wavefront of light as it passes through the SLM.

2.3 Holographic Displays

Holographic image formation models (e.g. [Lesem et al. 1969]) have been adapted to create digital holograms [Haugen et al. 1983] quite early in the history of phase SLMs. Holographic projection systems have been proposed in many flavors for research and specialty applications including pocket projectors [Buckley 2008]. Some projection systems use diffraction patterns addressed on a Ferroelectric Liquid Crystal Displays (FLCD) in combination with temporally and spatially coherent light for image generation. The challenges in holography for projectors lie in achieving sufficiently good image quality. Since holograms are optimized in the Fourier domain, the resulting phase masks exhibit very high spatial frequencies, which severely limits the diffraction efficiency, especially when combined with low-resolution and/or binary phase modulators. By comparison, we note that our method is not based on Fourier optics (in fact it follows a geometric optics image formation model), and generates phase masks that are piecewise smooth spatially, similar to a Fresnel lens.

2.4 Freeform Lenses

Recently there has been increased interest in freeform lens design, both for general lighting applications (e.g. [Miñano et al. 2009]) and for goal-based caustics [Berry 2006; Hullin et al. 2013]. In the latter application, we can distinguish between discrete optimization methods that work on a pixelated version of the problem (e.g. [Papas et al. 2011; Papas et al. 2012; Yue et al. 2012]), and those that optimize for continuous surfaces without obvious pixel structures (e.g. [Finckh et al. 2010; Kiser et al. 2013; Pauly and Kiser 2012; Schwartzburg et al. 2014; Yue et al. 2014]). The current state of the art methods define an optimization problem on the gradients of the lens surface, which then have to be integrated into a height field. This leads to a tension between satisfying a data term (the target caustic image) and maintaining the integrability of the gradient field.

In our previous work [2015] a simplified new formulation is derived in which the authors optimize directly for the phase function (i.e. the shape of the wavefront in the lens plane), or, equivalently, the lens shape, without a need for a subsequent integration step. This is made possible by a new parameterization of the problem that allows to express the optimization directly in the lens plane rather than the image plane. The formulation, which is summarized in Section 3.2, also serves as the basis for the development of our new realtime algorithm (Section 4).

2.5 Lens and Phase Function Equivalence

The effects of phase delays introduced by a smooth phase function can be related to an equivalent, physical refractive lens under the paraxial approximation, which can be derived using either geometric optics or from the Huygens principle. The paraxial approximation is widely used in optics and holds when $\sin\theta \approx \theta$. For the projection system considered in this paper, $|\theta| \leq 12°$, which corresponds to redirecting light from one side of the image to the other. The error in the paraxial approximation is less than 1% for this case, which makes optimizing directly for the phase surface possible.

3. BACKGROUND

3.1 HDR Luminance Requirements in Cinema

Little high brightness HDR video content is publicly available that has been color graded for a theatrical viewing environment. Partially this is of course due to the current lack of sufficiently capable large screen projection systems. In this section we attempt to estimate the relative power required to reproduce HDR luminance levels up to 10X above current peak luminance in cinema using color graded HDR still images. An analysis of 104 HDR images has been performed, and power requirements for a light steering projector as in the proposed architecture has been estimated. In this theoretical exercise it was found that a light steering projector with less power than a traditional cinema projector can directly reproduce all images up to $48cd/m^2$ and almost all of the surveyed HDR images up to $480cd/m^2$ without the need for additional tonal compression. Table I summarizes the results.

3.1.1 *Methodology.* Mark Fairchild's [2007] set of 104 scene-referred HDR images was analyzed (see Figure 1 for examples). The images differ in dynamic range from less than $1,000 : 1$ to over $10^9 : 1$. Most images are outdoor scenes. While the image data represents measured, scene-referred HDR (actual scene luminance levels) and is not intended for viewing on a cinema projector, an initial guess for a cinema-suitable rendering can be established by shifting the image intensity, so that the APL approximately matches the estimated viewer adaptation level in cinema. A simple linear scaling operator, $S_{adaptation}$, was determined manually for each image. Images were hand-tuned in a dark viewing environment, on a calibrated 27″ reference monitor (Dell U2713HMt, calibration confirmed using a Photo Research Inc. PR-650 spectro-radiometer) which was set to a peak white luminance of $48cd/m^2$ (D65 white point). While adjusting the intensity the images were viewed from a distance of approximately 3-5 screen-heights.

Fig. 1: Examples from the image set that was used in this study.

Once an adequate brightness scaling factor had been determined, luminance levels above 10x that of full-screen white (FSW), $480cd/m^2$, were clipped. Next, the steering efficiency of the proposed projector architecture was accounted for via a system PSF approximation (in this case a somewhat conservative, large Gaussian kernel spanning effectively 81 pixels of 1920 horizontal image pixels). The mean intensity across all pixels of the resulting luminance profile serves as an approximate metric for power requirements of a light steering projector.

3.1.2 *Computational steps:*

—Compute scaled luminance: $Y_s = Y_{hdr} \times S_{adaptation}$
—Clip Y_s to $10 \times 48cd/m^2 = 480cd/m^2$: $Y_{sc} = min(480, Y_s)$
—Account for steering efficiency: $Y_{scm} = Y_{sc} * g$
—Determine arithmetic mean luminance: $\bar{Y}_{scm} = mean(Y_{scm})$
—Scale to reference ($48cd/m^2$): $P_{rel} = \frac{\bar{Y}_{scm}}{48cd/m^2}$

3.1.3 *Results.* Figure 2 shows the estimated power required to reproduce each HDR image on a light steering projector with peak luminance identical to that of a traditional cinema projector, $48cd/m^2$, and of a light steering projector with a peak luminance one order of magnitude greater than cinema reference systems: $480cd/m^2$. All images can be reproduced on the $48cd/m^2$ light steering architecture using only a fraction of the power (13%) of a traditional projector. More importantly, almost all images can be reproduced up to $480cd/m^2$ (10x higher peak luminance) using the same or less power compared to a traditional projector.

We note that the APL of our data set when using the scale and clip operations described above with no further artistic color corrections appears higher than what might be expected from cinema-ready high brightness HDR content. We point the interested reader to [Zink and Smith 2015] for a recent introduction to HDR content production in which significantly lower APL's (3% and less) have been reported. This in turn would suggest that the power requirements for a light steering projector architecture could be even lower (or peak luminance and contrast higher) than proposed in our work. For our comparisons on the HDR prototype projector in Section 5 we select test images within a range of relatively conservative (=high) APLs from 7% - 45% (see Table III, second column).

Table I. : Power required to reproduce the images from the HDR data set on three different projectors (relative to a standard cinema projector in the first row).

L_{peak}	Steering?	P_{rel} (min)	P_{rel} (median)	P_{rel} 90%tile
$48cd/m^2$	no	1	1	1
$48cd/m^2$	yes	0.0107	0.1079	0.2595
$480cd/m^2$	yes	0.0107	0.1832	0.8554

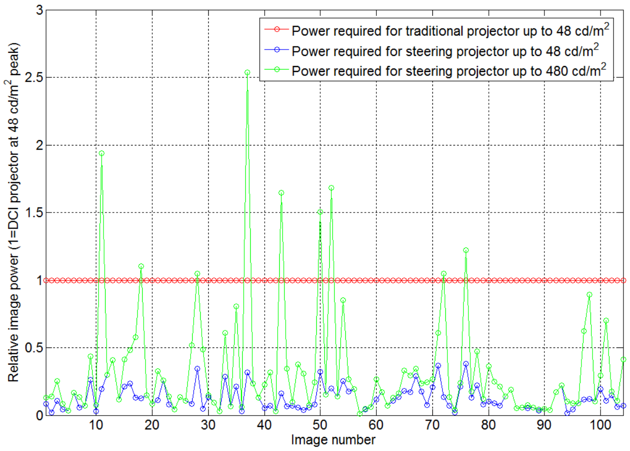

Fig. 2: Relative power required to reproduce each of 104 HDR images on three hypothetical projectors: two light steering projectors with a peak luminance of $48cd/m^2$ (blue) and $480cd/m^2$ (green) relative to a traditional, light blocking cinema projector with peak luminance of $48cd/m^2$ (red). The average power required to achieve identical peak luminance ($48cd/m^2$) is on the order of 13% of a traditional projector. More importantly, all but the very brightest images (approximately 9% of all images under test), can be re-produced up to a peak luminance of $480cd/m^2$ while using less or the same amount of power.

3.2 Freeform Lensing

In this section, we briefly summarize the basic freeform lensing algorithm [2015]. The new algorithmic contributions will then be presented in Section 4.

The basic geometry for freeform lensing using a phase modulator is depicted in Figure 3. A lens plane and an image plane (e.g. a screen) are placed parallel to each other at focal distance f. Collimated light is incident at the lens plane from the normal direction, but a phase modulator (or lens) in the lens plane distorts the phase of the light, resulting in a curved phase function $p(\mathbf{x})$, corresponding to a local deflection of the light rays.

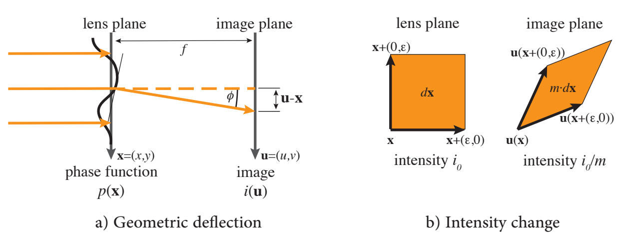

Fig. 3: Left: Geometry for the image formation model, with phase modulation $p(\mathbf{x})$ taking place in the lens plane, and resulting deflections creating a caustic image on the image plane at distance f. Right: The local intensity on the image plane is related to the change in the differential surface area between corresponding patches on the lens plane and the image plane.

Using the *paraxial approximation* $\sin\phi \approx \phi$, which is valid for small deflection angles, it is possible to show that the geometric displacement in the image plane is proportional to the gradient of the phase function:

$$\mathbf{u}(\mathbf{x}) = \mathbf{x} + f \cdot \nabla p(\mathbf{x}). \tag{1}$$

Likewise, the local intensity of a differential patch on the image plane is determined by the magnification (change in area) between this patch and the corresponding patch on the lens plane (Figure 3, right). This magnification factor $m(.)$ is related to the Laplacian of the phase modulation:

$$m(\mathbf{x}) \approx 1 + f \cdot \nabla^2 p(\mathbf{x}). \tag{2}$$

This yields the following expression for the intensity distribution on the image plane:

$$i(\mathbf{x} + f \cdot \nabla p(\mathbf{x})) = \frac{1}{1 + f \cdot \nabla^2 p(\mathbf{x})}. \tag{3}$$

In other words, the intensity $i(\mathbf{u})$ on the image plane can be directly computed from the Laplacian of the scalar phase function *on the lens plane*.

This image formation model gives rise to the following optimization problem for determining the phase function $p(\mathbf{x})$ for a given target image $i(\mathbf{u})$:

$$\begin{aligned}\hat{p}(\mathbf{x}) &= \underset{p(\mathbf{x})}{\arg\min} \int_{\mathbf{x}} \left(i_p(\mathbf{x}) - 1 + f \cdot \nabla^2 p(\mathbf{x})\right)^2 d\mathbf{x} \\ &= \underset{p(\mathbf{x})}{\arg\min}\, F(p(\mathbf{x}))\end{aligned} \tag{4}$$

where i_p is a *warped image* $i_p(\mathbf{x}) = i(\mathbf{x} + f \cdot \nabla p(\mathbf{x}))$ in which the target intensity $i(\mathbf{u})$ in the image plane has been warped backwards onto the lens plane using the distortion $\mathbf{u}(\mathbf{x})$ produced by a given phase function $p(\mathbf{x})$. This optimization problem can be solved by iterating between updates to the phase function and updates to the warped image. Convergence of the algorithm is moderate, so that the method is not directly suitable for realtime freeform lensing in projection systems.

The computational cost of the algorithm is primarily related to the solution of large-scale biharmonic problems. A Krylov subspace method (QMR) is employed making it difficult to find an effective preconditioner. The large scale of the system can also be problematic. Efficient solutions to biharmonic systems is an ongoing topic of research, including, for example, preconditioning approaches [Silvester and Mihajlović 2004], multigrid methods [Zhao 2004] and operator splitting schemes [Tang and Christov 2006]. Scaling these approaches to the millions of degrees of freedom which are required for imaging applications in realtime is challenging.

In the following section, we introduce a new approach based upon *proximal operators* that allow the problem to be expressed in the Fourier domain and consequently solved efficiently using highly parallelizable fast Fourier transform libraries.

4. REAL-TIME FREEFORM LENSING

The key insight is that by mirror padding the input image the system arising from the discretization of ∇^4 results in periodic boundary conditions with pure-Neumann boundary conditions at the nominal image edge. This is illustrated in Figure 4 and was also observed in earlier work by Ng et al. [1999] for deblurring images, but has not been exploited for lensing. The modification allows the product $\nabla^4 p$ in the objective function, Equation 4, to be expressed as a convolution via the Fourier convolution theorem since the system matrix resulting from discretizing Equation 4 is circulant. This enables the use of faster Fourier-domain solves in place of slower general purpose iterative linear solvers.

We build upon the method summarized in Section 3.2 and note that for periodic boundary conditions, this problem can be solved very efficiently in Fourier-space by using *proximal operators* [Parikh and Boyd 2013]. Proximal methods from sparse optimization allow for regularization to be imposed without destroying the structure of the system.

The specific proximal method that we use is a non-linear variant (Algorithm 1) of the well-known *proximal point method*. The proximal point method is a simple fixed-point iteration defined by Equation 5, that is expressed in terms of the *proximal operator*, $\mathrm{prox}_{\gamma F}(p(\mathbf{x}))$, of the objective function $F(p(\mathbf{x}))$.

$$p^{k+1}(\mathbf{x}) \leftarrow \mathrm{prox}_{\gamma F}(p^k(\mathbf{x})) \tag{5}$$

For an arbitrary convex function, $F(q(\mathbf{x}))$, the proximal operator, $\mathrm{prox}_{\gamma F}$, (defined in Equation 6) acts like a single step of a trust region optimization in which a value of $p(\mathbf{x})$ is sought that reduces F but does not stray too far from the input argument $q(\mathbf{x})$:

$$\mathrm{prox}_{\gamma F}(\mathbf{q}) = \arg\min_{\mathbf{p}} F(\mathbf{p}) + \frac{\gamma}{2}\|\mathbf{p}-\mathbf{q}\|_2^2. \tag{6}$$

To simplify notation, we use bold lower-case letters to refer to raster images, i.e. $\mathbf{p} = p(\mathbf{x})$, noting that there is an implied discretization step. The parameter γ serves to trade off the competing objectives of minimizing F while remaining close (proximal) to $\mathbf{q}$ but for strictly convex objectives does not affect the final solution, only the number of iterations required to reach it.

For a least-squares objective $F(\mathbf{p}) = \frac{1}{2}\|\mathbf{A}\mathbf{p}-\mathbf{b}\|_2^2$, the resulting proximal operator [Parikh and Boyd 2013] is found by expanding the resulting right hand side from Equation 6 and setting the gradient of the minimization term to zero. This results in Equation 7:

$$\mathrm{prox}_{\gamma F}(\mathbf{q}) = \left(\gamma + \mathbf{A}^T\mathbf{A}\right)^{-1}\left(\gamma\mathbf{q} + \mathbf{A}^T\mathbf{b}\right). \tag{7}$$

In our case, the function F is simply the integral term from Equation 4. We form the proximal operator by discretizing the integral with sums over image pixels and defining: $\mathbf{A} = f\nabla^2$ and $\mathbf{b} = 1 - i_p(\mathbf{x})$.

Since proximal operators contain a strictly convex regularization term, $\|\mathbf{p}-\mathbf{q}\|_2^2$, the whole operator is a strictly convex function even if F is only weakly convex, as is the case for our problem. The proximal regularization improves the conditioning of our problem and can be interpreted as *disappearing Tikhonov regularization* [Parikh and Boyd 2013], i.e. regularization whose effect diminishes to zero as the algorithm converges. This is helpful since the added regularization does not distort the solution.

Another benefit is that the proximal regularization does not change the structure of our problem since it only adds an identity term. This, coupled with the mirrored padding periodic boundary conditions, means that all terms in Equation 4 can be expressed as convolutions and the proximal operator solved in the Fourier domain. This is vastly more efficient than solving the optimization implied by the proximal operator in the spatial domain.

By denoting the forward and inverse Fourier transforms as $\mathcal{F}()$ & $\mathcal{F}^{-1}()$ respectively, complex conjugation by $*$ and performing multiplication and division point-wise, the proximal operator for Equation 7 can be re-expressed in the Fourier domain as Equation 8 for circulant matrices $\mathbf{A}$, as reported in [Chambolle and Pock 2011] who used it to solve deconvolution problems.

$$\mathrm{prox}_{\gamma F}(\mathbf{q}) = \mathcal{F}^{-1}\left(\frac{\mathcal{F}(\mathbf{b})\mathcal{F}(\mathbf{A})^* + \gamma\mathcal{F}(\mathbf{q})}{\mathcal{F}(\mathbf{A})^2 + \gamma}\right) \tag{8}$$

In practice, we modify Equation 8 slightly by the addition of a regularization parameter α that favors low-curvature solutions. The modified proximal operator is shown in Equation 9.

$$\mathrm{prox}_{\gamma F}(\mathbf{q}) = \mathcal{F}^{-1}\left(\frac{\mathcal{F}(\mathbf{b})\mathcal{F}(\mathbf{A})^* + \gamma\mathcal{F}(\mathbf{q})}{(1+\alpha)\mathcal{F}(\mathbf{A})^2 + \gamma}\right) \tag{9}$$

The constant $\alpha \geq 0$ regularizes the solution by favoring results with low curvature. This corresponds to solving a modified form of Equation 4 that imposes a penalty of $\frac{\alpha}{2}\|\nabla^2 p(x)\|^2$ once discretized (the second term of Equation 10 in the continuous case).

$$\begin{aligned}\hat{p}(\mathbf{x}) \;=\; & \arg\min_{p(\mathbf{x})} \int_{\mathbf{x}} \left(i_p(\mathbf{x}) - 1 + f\cdot\nabla^2 p(\mathbf{x})\right)^2 d\mathbf{x} \\ & +\; \alpha\int_{\mathbf{x}} \left(\nabla^2 p(\mathbf{x})\right)^2 d\mathbf{x},\end{aligned} \tag{10}$$

The effect of the parameter α is to favor smoother solutions than can otherwise be found. This helps to prevent the method from producing undesirable caustics in an attempt to achieve very bright highlights at the expense of image quality in darker regions. The effect of the α parameter is shown in Figure 5 for lens simulations.

Our final algorithm is shown in Algorithm 1 and is identical to the proximal point method except that the $\mathbf{b}$ image used by the proximal operator is updated at every iteration using the warping procedure from our previous work [2015]. After precomputing the Fourier transforms of $f\nabla^2$, each iteration of the algorithm can be implemented with an image warping, some component-wise operations and a forward/inverse Fourier transform.

Algorithm 1 Paraxial caustics in Fourier space

// Initialize phase surface as a constant value
$p^0(\mathbf{x}) \leftarrow 0$
// Initialize iteration counter and constant parameters
$\mathbf{A} \leftarrow f\nabla^2$
$k \leftarrow 0$
while $k < k_{\max}$ **do**
  // Warp target image by current solution
  $i_p^k(\mathbf{x}) \leftarrow i(\mathbf{x} + f\nabla p^k(\mathbf{x}))$
  // initialize right hand side of least-squares problem
  $\mathbf{b} \leftarrow 1 - i_p^k(\mathbf{x})$
  // Update the current solution by evaluating
  // the proximal operator in Equation 9
  $p^{k+1}(\mathbf{x}) \leftarrow \mathrm{prox}_{\gamma F}(p^k(\mathbf{x}))$
  // update iteration index
  $k \leftarrow k + 1$
end while
// RETURN computed mapping
return $p^{k_{\max}}(\mathbf{x})$

4.1 Implementation

The re-formulation of the algorithm results in orders of magnitude speedup when executed on a CPU using FFT based solvers over the QMR solver that was previously used. Typical per-frame computation times were previously on the order of 20 minutes or more [2015], while the Fourier version in Algorithm 1 takes approximately 0.6 seconds at the same resolution (256 × 128) on a Core i5 desktop computer, a speedup of approximately 2,000 times. The conversion to Fourier domain solves also results in operations that are more friendly for parallel GPU implementation. We have implemented the algorithm both in C++ and in CUDA using CUFFT for the forward and inverse Fourier transforms [NVIDIA 2015]. The CUDA & CUFFT version of the code yields nearly a 150 times speedup over the single-threaded CPU version when run on a GeForce 770 GPU, resulting in roughly a 300,000 fold speedup over the naive CPU version implemented using QMR. To our knowledge this makes the algorithm the first freeform lensing method capable of operating in real-time, see Table II. This is in contrast to methods such as [Schwartzburg et al. 2014], which produce very high quality results, but have runtimes roughly five orders of magnitude higher than our GPU algorithm.

Table II. : Runtimes for various resolution inputs with 10 iterations of Algorithm 1

Algorithm	Resolution	Runtime (ms)	FPS
CPU	256×128	600ms	1.7
GPU	256×128	4ms	250
GPU	480×270	14ms	71
GPU	960×540	52ms	19
GPU	1920×1080	212ms	4.7

The algorithm is well suited to hardware implementation on devices such as GPUs, FPGAs or ASICs due to its use of highly parallel FFTs and component-wise operations. We run Algorithm 1 for a fixed number of iterations (typically 10 or less). Convergence to a solution is rapid, requiring well fewer than 10 iterations, however for many hardware implementations it is desirable to have computation times that are independent of frame content.

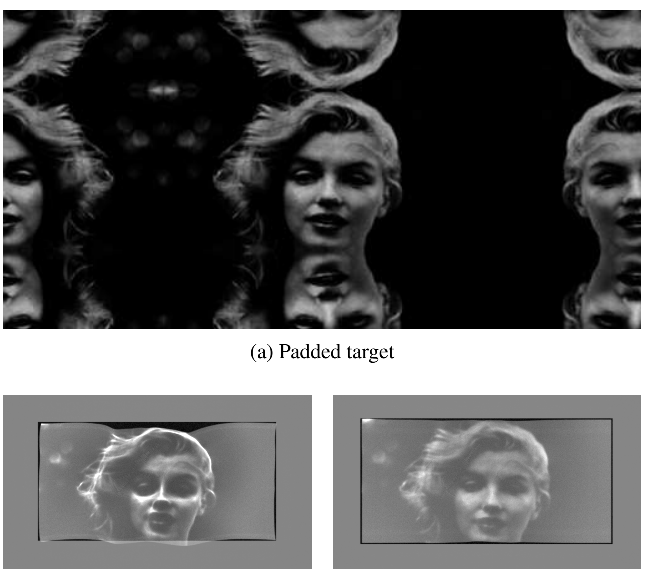

(a) Padded target

(b) Without padding

(c) Mirrored padded

Fig. 4: By mirror-padding the input image, pure-Neumann boundary conditions at the image edge can be achieved while retaining a Toeplitz matrix structure. This prevents distortions of the image boundary. Results were simulated with LuxRender.

4.2 Simulation Results

Using the equivalence between physical lenses and phase functions allows solid lens models to be generated for testing via geometric optics simulation (we use Blender+LuxRender). Examples are shown in Figure 4 and 5 which illustrate the effect of mirror padding and the choice of α respectively.

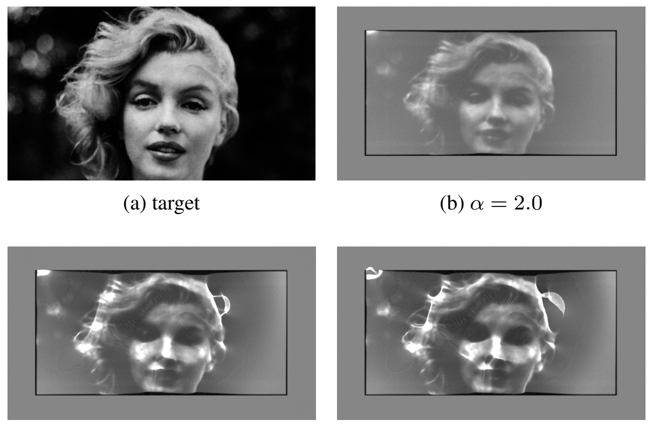

(a) target

(b) $\alpha = 2.0$

(c) $\alpha = 0.2$

(d) $\alpha = 0.02$

Fig. 5: LuxRender raytracing simulations: the smoothness parameter α penalizes strong caustics in the image that achieve high-brightness but poor image quality.

4.3 Static Phase Plates

We evaluate a selection of phase patterns using static phase plates with dimensions comparable to that of a phase-only SLM (approximately 12mm x 7mm). Figure 6 shows two phase plates that were manufactured on a fused silica wafer using a lithography based process as well as the resulting light fields when illuminated with a collimated laser beam. The spatial resolution of the phase pattern is high at 12,288 x 6912 pixels per lens ($1.00\,\mu$m pixel pitch). The phase resolution was limited to 8 phase levels (4 masks in the lithography process resulted in 8 phase levels between 0 and 2 pi). The static phase plates were manufactured to evaluate our freeform lenses for static beam shaping applications and to test the method on high power in this case fiber coupled lasers in which spatial coherence properties are partially destroyed. The laser used for experiments (see results in Figure 6) is a 638nm laser with up to 60W optical power. A suitable lens is used to expand the beam and to provide an approximately collimated (but slightly diverging) beam of light to illuminate the phase plates. Spatial coherence is partially destroyed as multiple laser sources within the module are combined and coupled into a $400\,\mu$m fiber which integrates light traveling along multiple light paths. The ability to focus light from this source perfectly is limited (this applies not only to our phase plates, but also to ordinary glass lenses and other optics), and thus the sharpness of the resulting image is affected. For the proposed use case as a structured light source in a projection system, a small amount of blur in the image is acceptable, if not desirable. The raytracing simulations in Section 4.2 begin with a model of a near-perfectly collimated light source (a distant point light source) and are therefore sharper than the image produced by our experimental

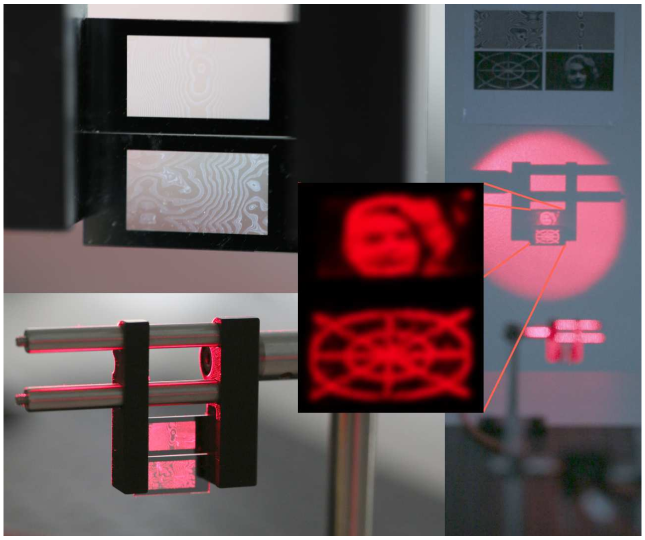

Fig. 6: Static phase plates manufactured on a fused silica wafer for two test patterns (Marilyn and Align). Left: phase plates without and with laser illumination. The top phase plate reproduces *Marilyn*, the lower phase plate focuses the *Align* pattern. Right: The fiber-coupled and beam expanded laser light source as well as two phase plates mounted in the light path (out of focus in the photo) are shown in the foreground. The projected structured illumination pattern is focused on the screen. For reference, above the red projection is a printed copy of the phase pattern etched into the wafer as well as a print-out of a wave-front simulation of the expected intensity distribution on screen. The light pattern visually matches the simulation well.

phase plate (due to divergence of the beam). However, the overall geometry of the experimental light distribution appears visually undistorted and the image contrast is comparable to that of the simulations. For the projector prototype described in Section 5 we use a free space laser and achieve a similar amount of blur with a diffuser.

5. DYNAMIC LENSING IN PROJECTION SYSTEMS

In order to apply the freeform lens concept in projection displays, we require a spatial light modulator that can manipulate the shape of the wavefront of reflected or transmitted light. We first provide a brief overview of the different technologies available for this purpose, and then describe experiments and prototypes using the technology.

There are several commercially available technologies that can rapidly manipulate the phase of an incident wavefront in order to modulate phase. These include microelectromechanical (MEMS) displays such as analog mirror arrays [Hoskinson et al. 2012] or deformable mirrors used in wavefront sensing and correction. The benefit of MEMS based devices is the very fast temporal response. Disadvantages include cost and availability as well as the relatively low spatial resolution: devices with 4096 actuators are considered high resolution in this domain, leaving a resolution gap of 3 orders of magnitude to common projection displays.

An alternative to MEMS based mirrors is offered by liquid crystal displays either in form of a transmissive LCD or in a reflective configuration: liquid crystal on silicon (LCoS). Liquid crystal displays can retard the phase of light and offer high spatial resolution. Reflective LCoS devices can update at higher switching speeds compared to transmissive LCD due to the reduced cell gap, and also provide a high pixel fill factor. Omitting the input/output polarizing beam splitter and carefully managing the polarization state of incoming light allows for the operation in phase-only mode, in which phase is retarded based on the rotation amount of the liquid crystals at each pixel location. Although standard LCoS modules can in principle be used as phase modulators, dedicated displays are available that can be calibrated to shift phase by one wavelength or more which allows for the implementation of "steeper" lenses that steer light more aggressively. The pixel values of the LCoS module then correspond directly to the wavelength modulated phase function, i.e. $\mathrm{mod}(p(x), \lambda)$. For more on this topic we refer the reader to [Robinson et al. 2005].

Our choice of phase SLM is a reflective Liquid Crystal on Silicon (LCoS) chip distributed by [Holoeye Photonics AG 2015]. It provides a spatial resolution of 1920x1080 pixels at a pixel pitch of $6.4\mu m$, and can refresh at up to 60Hz. Access to a look-up-table allows for calibration of the modulator for different working wavelengths. The fill factor and reflectivity of the display are high compared to other technologies at 93% and 75% respectively. The phase retardation is calibrated to between 0 and 2π, equivalent to one wavelength of light.

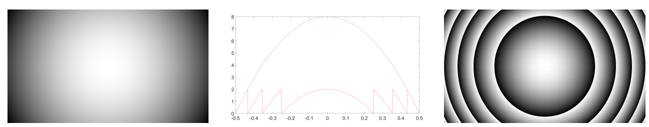

(a) 8π spherical lens (b) cross section (c) wrapped at 2π

Fig. 7: *Phase wrapping* example: a) phase function of a spherical lens with a height of 8π, b) a plot of the cross section of the original and the phase wrapped lens, and c) the same lens wrapped at intervals of 2π.

This is sufficient to generate freeform lenses with a long focal distance. For shorter focal distances, we require more strongly curved wavefronts, which creates larger than 2π values for $p(.)$. We can address this issue by *phase wrapping*, i.e. using the fractional part of $p(.)$ to control the SLM which results in patterns similar to a Fresnel lens. A simple example to demonstrate this technique is presented in Figure 7 (also see red box in Figure 8 as well as the phase patterns in Figures 11 and 12).

5.1 Prototype

We initially analyze results from the first (phase) modulation stage in isolation (see Figure 8) and later relay the resulting light profile into the second stage for amplitude attenuation. The intermediate results that can be seen in Figure 11 are a product of tuning the type and position of the diffuser in the setup in Figure 8. Later, the simple projection lens in Figure 8 was replaced with a relay lens with an appropriate focal distance to couple the diffused light profile into the projection head (also see Figure 9).

The use of single mode lasers causes small-scale artifacts including screen speckle and diffraction *fringes* due to interference (Figure 11, center photo). Artifacts of this nature can be reduced below the visible threshold by using for example a different type of laser light source (as for example in Section 4.2), or a set of lasers with different center wavelengths, or broadband light sources such as LEDs and lamps as used in our previous work [2015]. When constrained to using a narrow band laser light source such as in our test setup, a similar image *smoothing* effect can be achieved

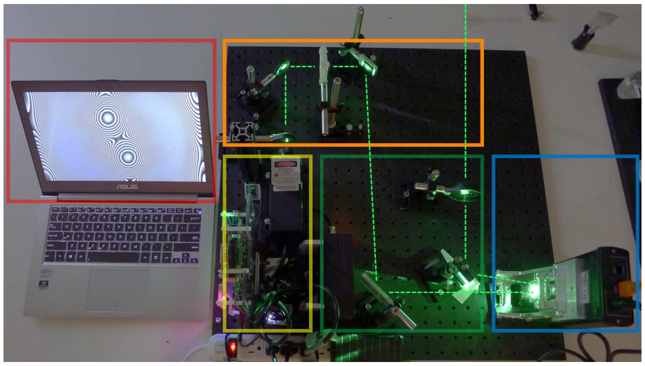

Fig. 8: Phase modulation test setup consisting of a light source (yellow box, 532nm DPSS laser and laser controller), beam expansion and collimation optics and folding mirrors (orange box), the reflective phase SLM (blue), various folding mirrors and a simple projection lens to relay the image from and intermediate image plane onto the projection screen (green). The image is formed in an intermediary image plane between the phase modulator and the projection lens. We empirically determine the type and position of a diffuser (not depicted) close to this intermediate image plane to produce the light profile in Figure 11. The gray scale intensity of the phase pattern shown on the computer screen correlates linearly to the desired phase retardation in the optical path to form the image. This pattern has been phase-wrapped at multiples of one wavelength and can be addressed directly onto the micro display.

by spatially or temporally averaging the image using for example a diffuser or commercially available continuous deformable mirrors that introduces slight angular diversity in a pseudo-random fashion at high speeds. For ease of implementation we choose a structured (holographic) diffuser with half angle of 0.5° which is placed in an intermediate image plane following the phase SLM. Such diffusers are available at high transmission efficiencies of $> 90\%$. A photo of the *cleaned-up* intensity profiles can be seen in Figure 11, right.

At a high level, the light path of a traditional projection system consist of a high intensity light source and some form of beam shaping: for example beam expansion, collimation and homogenization, color separation and recombining optics. At the heart of a typical projector, a small SLM attenuates the amplitude of light per pixel. The resulting image is then magnified and imaged onto the projection screen. We integrate the laser light source as well as the phase-only modulation stage and diffuser into the architecture of an existing projector and demonstrate a high brightness, high dynamic range projection system, in which a structured light field is formed based on the new dynamic lensing method. Additional sharpness and contrast is provided using a traditional LCoS-based amplitude modulating micro display.

We make use of the forward image formation model from our simulations to predict the illumination profile present at the second, amplitude-only modulator. Given the phase function from the freeform lensing algorithm, the light distribution on the image plane is predicted using the simple model from Equations 1 and 2. The amount of smoothness introduced at the diffuser at the intermediate image plane can be modeled using a blur kernel (system point spread function that can be either directly measured or computed via deconvolution for known targets) and the modulation pattern required for the amplitude modulator is then obtained to introduce any missing spatial information as well as additional contrast where needed. We note that careful calibration and characterization of the

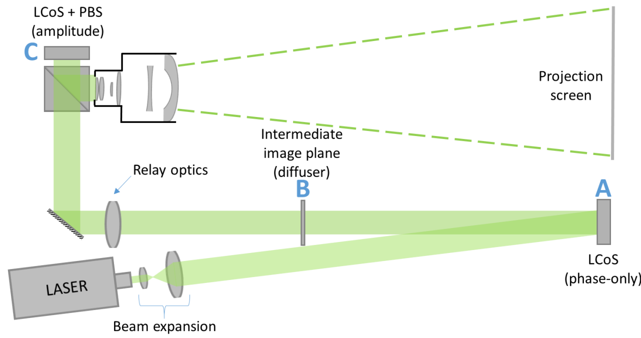

Fig. 9: System diagram of the proposed and prototyped high brightness, HDR projector: light from an expanded and collimated laser beam is reflected off a phase-only modulator (A). The per-pixel amount of phase retardation resembles the height field of the dynamic lens calculated with our algorithm. The effective focal plane of this freeform lens is in-plane with a diffuser (B) which in turn is relayed onto the image plane of an off-the-shelf, reflective projection head (C) consisting of the polarizing beam splitter together with an LCoS microdisplay and a projection lens. Light from dark parts of the image can be used to create high luminance features, and simultaneously reduce the black level.

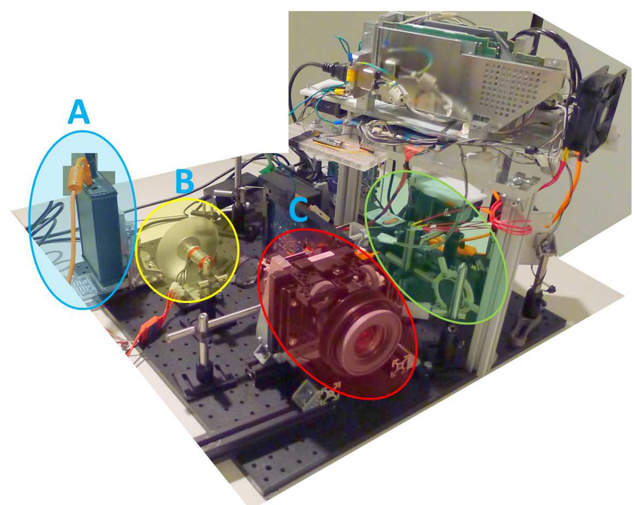

Fig. 10: Prototype system used for results photographs in Figures 11 and 12 including laser light source and both the light steering as well as the amplitude modulation stage. Positions A (blue, phase modulator), B (yellow, diffuser) and C (red, amplitude modulation and projection optics) correlate to the positions labeled in Figure 9. The green marked area holds the laser light source, the remainder of the photos is mounting hardware and control electronics.

entire optical system is required to optimally control the SLMs. No significant efforts beyond careful spatial registration of the two images (illumination profile caused by phase retardation and amplitude modulation on the SLM) and calibration to linear increments in light intensity were performed for this work.

5.2 Results

Figure 11 shows the phase patterns computed by Algorithm 1 as applied to the phase modulator with black corresponding to no

Fig. 11: From left to right correlating to positions A to C in Figure 9: A: phase pattern present at phase-only LCoS modulator, B: direct image produced by lens in intermediary image plane (prior to diffuser) and C: intensity distribution present at amplitude LCoS modulator after having passed through a thin diffuser.

phase retardation and white corresponding to a retardation of 2π. We illustrate how phase patterns with maximum phase retardation larger than 2π can be wrapped to the maximum phase retardation of the modulator, resulting in a pattern similar to a Fresnel lens. The resulting light profile resembles the target image closely, but also contains a small amount of local, high spatial frequency noise. We make use of a high transmission efficiency patterned diffuser (0.5° half-angle) to integrate over these local intensity variations. The resulting light profile at the diffuser is locally smooth and still provides sufficient contrast to enhance peak luminance and lower black level significantly.

Figure 12 shows a selection of experimental results for our method. The first row of Figure 12 shows the phase pattern addressed onto the phase SLM. In the second row of Figure 12 we show photos of the light steering high brightness projector and compare them to what a traditional projector with the same lumen rating out of lens would look like (third row). For the latter case we simply address a flat phase across the phase SLM. The last two rows show false-color logarithmic luminance plots on the same scale for the traditional (bottom) and light steering projector (fourth row) systems. All photos were captured with identical camera settings and show that our method not only recovers better black levels but also allows for increased luminance of highlights by redistributing light from dark regions of the image to lighter regions making better use of available power and enabling high brightness high-dynamic range projection with drastically reduced power consumption. Table III contains measured black level and peak luminance data for both the LDR and HDR cases for each of the test images. The L_{peak} gain and contrast gain entries in the right columns summarize the merit of the proposed approach. While HDR images are unlikely to have as high of an APL as for example the second test image (48%), a gain in peak luminance of $3X$, while costly, might be feasible to produce with existing projection technologies (for example by using a high gain screen or a very high power light source). The black level of such a system would also be elevated by a factor of $3X$. Achieving a gain in L_{peak} of $10X$ - $15X$ (such as in some of the other test cases) using traditional projector technologies is not feasible, both because of light source power limitations and due to visibly elevated black levels. We note that the contrast numbers presented in the table represent the *in-scene* contrast rather than a sequential contrast.

5.3 Limitations and Future Work

The prototype architecture presented in this work and the resulting image quality improvements in contrast and peak luminance that can be achieved with it demonstrate the feasibility of the concept. We briefly want to discuss some of the obvious and less obvious limitations of the implementation. We believe that while non-trivial, most of these limitations can be addressed with a modest amount of further engineering work.

—The test system was built with a single, monochromatic (green) light source. For a full color projector, at least two additional color channels will need to be added to the system in either a parallel or a time sequential fashion. Either approach presents its own (solved) challenges. The former with respect to alignment of red, green and blue components such as SLM and dichroic mirrors and the latter with respect to synchronization/timing and thermal limitations.

—As with any display based on narrow band or monochromatic light sources (such as LEDs or lasers) care needs to be taken to manage undesirable properties such as observer metamerism and speckle.

—The phase SLM and the amplitude SLM need to be synchronized, ideally at the frame or subframe level. The amplitude modulator in the prototype was borrowed from a consumer projector which introduced an undesired latency in one of the modulation stages.

—In a full color system sufficient colorimetric calibration will only be possible by characterizing and accurately modeling the system, including the PSF, which depending on the light source and optical path could potentially be dependent on location or even feature size.

—None of the relay optics or other elements were custom designed for the prototype, which leads to light losses. Even with a more optimized light path, the addition of a phase SLM can reduce the overall light throughput. We estimate that this loss can be as high as 40-60% for the components used in the prototype. While this might seem high we note that even for bright images (APL of 50%) the gain in peak luminance exceeds what could be achieved in a traditional projector. Better suitable SLMs can further reduce the associated light losses.

—Careful alignment of a number of elements in the light path is required to achieve a uniform and predictable light profile on the phase modulator. In our experiment, the reflective nature of the phase SLM required off-axis illumination that was not accounted for in the simulations and algorithm and which in turn leads to errors in the resulting luminance profiles. While these errors were not clearly visible in the images projected onto the screen, the logarithmic luminance representation in Figure 12 reveal this non-uniformity. It can be accounted for in the lens pattern.

—Finally, the dynamic nature of the projection system with respect to peak luminance and feature size may present a challenge when color grading content for the display. The notion of a limited light budget and a peak luminance that exceeds that of full screen white might makes sense from an HDR image statistics point of view, but would require a re-thinking in existing movie production processes.

6. DISCUSSION AND CONCLUSIONS

We have made two technical contributions: a simple but fast and effective new optimization method for freeform lenses (goal-based caustics), and a new dual-modulation design for projection displays, which uses a phase-only spatial light modulator as a programmable freeform lens for HDR projection.

The new freeform lens optimization approach is based on first-order (paraxial) approximations, which hold for long focal lengths and are widely used in optics. Under this linear model, the local deflection of light is proportional to the gradient of a phase modulation function, while the intensity is proportional to the Laplacian.

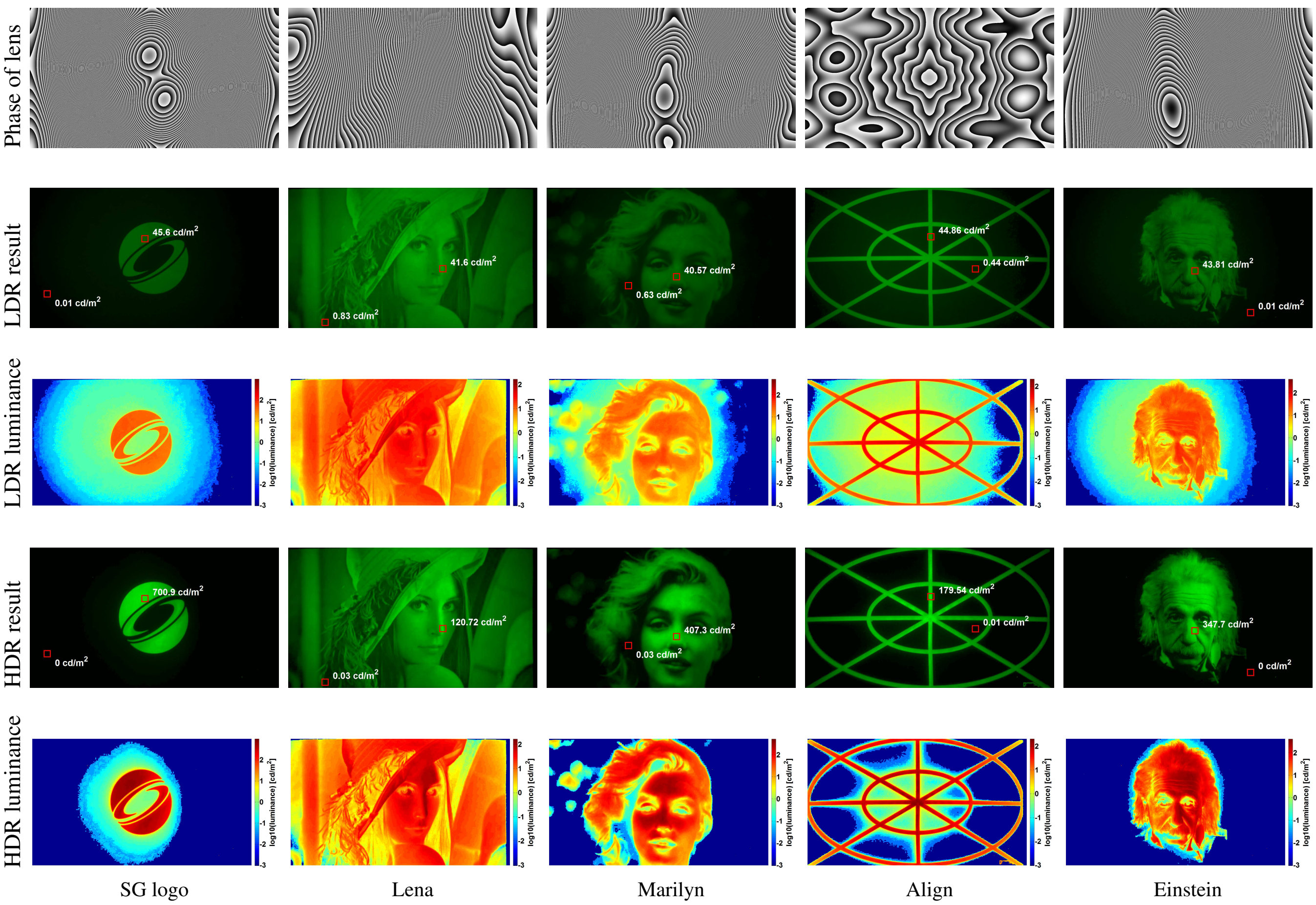

Fig. 12: Result photos and measurements of the HDR prototype projector. Top to bottom: *Phase Function of Lens* - the phase pattern as computed by Algorithm 1. *LDR projector for comparison* - the same projector power (out of lens) used in a traditional, light attenuating mode: a uniform light field (flat phase field) is provided to the amplitude SLM which forms the image by blocking light. *LDR luminance profile on a logarithmic scale*. *HDR projector* - photograph of our lensing approach used to redistribute light from dark regions to bright regions, resulting in improved black levels and significantly increased highlight intensity. *HDR luminance profile on a logarithmic scale*.

Table III. : Luminance measurements of the results depicted in Figure 12. Multiple exposures at varying exposure times were capture (8s, 4s, 2s, 1s, 1/2s, 1/4s, 1/8s, 1/15s, 1/30s, 1/60s, 1/125s) and combined into one linear HDR file, which was then calibrated to represent actual luminance values using a luminance spot meter (Minolta LS100). The lowest accurate measurement using the Minolta LS100 is 0.001 cd/m^2.

Name	Power (relative)	HDR L_{peak} $[cd/m^2]$	HDR L_{black} $[cd/m^2]$	HDR contrast	LDR L_{peak} $[cd/m^2]$	LDR L_{black} $[cd/m^2]$	LDR contrast	**L_{peak} gain**	**Contrast gain**
SG logo	7%	701	0.001	700900 : 1	46	0.01	4,272 : 1	**15X**	**173X**
Lena	48%	121	0.03	4053 : 1	42	0.83	50 : 1	**3X**	**80X**
Marilyn	23%	407	0.03	13008 : 1	41	0.63	64 : 1	**10X**	**203X**
Align	20%	180	0.01	29677 : 1	45	0.44	101 : 1	**4X**	**292X**
Einstein	15%	348	0.001	347700 : 1	44	0.01	2,996 : 1	**8X**	**122X**

We combine this insight with a new parameterization of the optimization problem *in the lens plane* instead of the image plane to arrive at a simple to implement method that optimizes directly for the phase function without any additional integration steps. Solved in the Fourier domain, this is the first algorithmic approach for freeform lensing that is efficient enough for on-the fly computation of video sequences.

Our new dual-modulation HDR projector design finally allows to achieve perceptually meaningful gains in peak luminance on large cinema screens while simultaneously improving black level performance and maintaining a manageable power, light and cost budget. As such we believe that to date the approach presents one of the most sensible proposals for commercial high contrast HDR projection systems and one of the most practical ways to achieve high brightness HDR imagery in cinema.

ACKNOWLEDGMENTS

The authors would like to thank Qiang Fu for spending many hours manufacturing the two static phase plates in the nanofab lab at KAUST and gratefully acknowledge Anders Ballestad's contributions to Section 3.1, especially the hand-tuning of all 104 HDR images to determine the appropriate scaling factors for dark viewing environments.

REFERENCES

BERRY, M. 2006. Oriental magic mirrors and the laplacian image. *European journal of physics 27,* 1, 109.

BIMBER, O. AND IWAI, D. 2008. Superimposing dynamic range. *ACM Trans. Graph. 27,* 5, 150.

BLACKHAM, G. AND NEALE, A. 1998. Image display apparatus. EP Patent App. EP19,970,306,624.

BUCKLEY, E. 2008. 70.2: Holographic laser projection technology. In *Proc. SID*. Vol. 39. 1074–1079.

CHAMBOLLE, A. AND POCK, T. 2011. A first-order primal-dual algorithm for convex problems with applications to imaging. *Journal of Mathematical Imaging and Vision 40,* 1, 120–145.

DAMBERG, G. AND HEIDRICH, W. 2015. Efficient freeform lens optimization for computational caustic displays. *Optics Express 23,* 8, 10224–10232.

DAMBERG, G., SEETZEN, H., WARD, G., HEIDRICH, W., AND WHITEHEAD, L. 2007. 3.2: High dynamic range projection systems. In *Proc. SID*. Vol. 38. Wiley Online Library, 4–7.

DAMBERG, G., SEETZEN, H., WARD, G., KANG, M., LONGHURST, P., HEIDRICH, W., AND WHITEHEAD, L. 2007. High dynamic range projector. *Siggraph Emerging Technologies*.

FAIRCHILD, M. D. 2007. The hdr photographic survey. In *Color and Imaging Conference*. Vol. 2007. Society for Imaging Science and Technology, 233–238.

FINCKH, M., DAMMERTZ, H., AND LENSCH, H. P. 2010. Geometry construction from caustic images. In *Proc. ECCV*. 464–477.

HAUGEN, P. R., BARTELT, H., AND CASE, S. K. 1983. Image formation by multifacet holograms. *Applied optics 22,* 18, 2822–2829.

HOLOEYE PHOTONICS AG. 2015. Holoeye corporation. *URL http://www. holoeye. com*.

HOSKINSON, R., HAMPL, S., AND STOEBER, B. 2012. Arrays of large-area, tip/tilt micromirrors for use in a high-contrast projector. *Sensors and Actuators A: Physical 173,* 1, 172–179.

HOSKINSON, R., STOEBER, B., HEIDRICH, W., AND FELS, S. 2010. Light reallocation for high contrast projection using an analog micromirror array. *ACM Transactions on Graphics (TOG) 29,* 6, 165.

HULLIN, M. B., IHRKE, I., HEIDRICH, W., WEYRICH, T., DAMBERG, G., AND FUCHS, M. 2013. State of the art in computational fabrication and display of material appearance. In *Eurographics Annual Conference (STAR)*.

KISER, T., EIGENSATZ, M., NGUYEN, M. M., BOMPAS, P., AND PAULY, M. 2013. Architectural Caustics: Controlling Light with Geometry. In *Advances in Architectural Geometry 2012*. Springer, 91–106.

KUSAKABE, Y., KANAZAWA, M., NOJIRI, Y., FURUYA, M., AND YOSHIMURA, M. 2009. A high-dynamic-range and high-resolution projector with dual modulation. *Proc. SPIE 7241*, 72410Q–72410Q–11.

LESEM, L., HIRSCH, P., AND JORDAN, J. 1969. The kinoform: a new wavefront reconstruction device. *IBM Journal of Research and Development 13,* 2, 150–155.

MIÑANO, J. C., BENÍTEZ, P., AND SANTAMARÍA, A. 2009. Free-form optics for illumination. *Optical Review 16,* 2, 99–102.

NG, M. K., CHAN, R. H., AND TANG, W.-C. 1999. A fast algorithm for deblurring models with neumann boundary conditions. *SIAM Journal on Scientific Computing 21,* 3, 851–866.

NVIDIA. 2015. Programming guide, cusparse, cublas, and cufft library user guides.{Online}.

PAPAS, M., HOUIT, T., NOWROUZEZAHRAI, D., GROSS, M., AND JAROSZ, W. 2012. The magic lens: refractive steganography. *ACM Transactions on Graphics (TOG) 31,* 6, 186.

PAPAS, M., JAROSZ, W., JAKOB, W., RUSINKIEWICZ, S., MATUSIK, W., AND WEYRICH, T. 2011. Goal-based caustics. *Computer Graphics Forum 30,* 2, 503–511.

PARIKH, N. AND BOYD, S. 2013. Proximal algorithms. *Foundations and Trends in Optimization 1,* 3, 123–231.

PAULY, M. AND KISER, T. 2012. Caustic art. Tech. rep.

REINHARD, E., POULI, T., KUNKEL, T., LONG, B., BALLESTAD, A., AND DAMBERG, G. 2012. Calibrated image appearance reproduction. *ACM Transactions on Graphics (TOG) 31,* 6, 201.

REMPEL, A., HEIDRICH, W., LI, H., AND MANTIUK, R. 2009. Video viewing preferences for hdr displays under varying ambient illumination. *Proc. APGV*, 45–52.

REMPEL, A., HEIDRICH, W., AND MANTIUK, R. 2011. The role of contrast in the perceived depth of monocular imagery. *Proc. APGV*, 115.

ROBINSON, M. D., SHARP, G., AND CHEN, J. 2005. *Polarization engineering for LCD projection*. Vol. 4. John Wiley & Sons.

SCHWARTZBURG, Y., TESTUZ, R., TAGLIASACCHI, A., AND PAULY, M. 2014. High-contrast computational caustic design. *ACM Trans. Graph. (Proc. Siggraph)*. (in print).

SEETZEN, H. 2009. High dynamic range display and projection systems. Ph.D. thesis, University of British Columbia.

SEETZEN, H., HEIDRICH, W., STUERZLINGER, W., WARD, G., WHITEHEAD, L., TRENTACOSTE, M., GHOSH, AND VOROZCOVS, A. 2004. High dynamic range display systems. *ACM Trans. Graph. (Proc. SIGGRAPH)*, 760–768.

SILVESTER, D. J. AND MIHAJLOVIĆ, M. D. 2004. A black-box multigrid preconditioner for the biharmonic equation. *BIT Numerical Mathematics 44,* 1, 151–163.

TANG, X. H. AND CHRISTOV, C. I. 2006. An operator splitting scheme for biharmonic equation with accelerated convergence. In *Proceedings of the 5th International Conference on Large-Scale Scientific Computing*. LSSC'05. Springer-Verlag, Berlin, Heidelberg, 387–394.

YUE, Y., IWASAKI, K., CHEN, B.-Y., DOBASHI, Y., AND NISHITA, T. 2012. Pixel art with refracted light by rearrangeable sticks. *Computer Graphics Forum 31,* 2pt3, 575–582.

YUE, Y., IWASAKI, K., CHEN, B.-Y., DOBASHI, Y., AND NISHITA, T. 2014. Poisson-based continuous surface generation for goal-based caustics. *ACM Trans. Graph.*. (in print).

ZHAO, J. 2004. Convergence of v-cycle and f-cycle multigrid methods for the biharmonic problem using the morley element. *Electronic Transactions on Numerical Analysis 17*, 112–132.

ZINK, M. AND SMITH, M. 2015. Managing HDR content production and display device capabilities. *International Broadcasting Convention 2015*.

Received July 2015; accepted December 2015